JOURNAL OF MATERIALS SCIENCE 29 (1994) 728–735

Laser-modified aluminium surfaces with iron

L. GJØNNES*, A. OLSEN
Center for Materials Research/Department of Physics, University of Oslo, P.O.Box 1048, 0316 Oslo, Norway

Possible improvements in the mechanical properties of surface-coated aluminium have been investigated. Aluminium plasma sprayed with iron powder was processed using two different laser-beam settings (integrated and defocused) with varying processing parameters. Mechanical and microstructural characterizations of the specimens revealed great differences between the two laser-beam settings. The defocused laser beam showed a clear improvement of hardness which was not observed for the integrated laser beam. The integrated laser beam gave deep melt pools with large Al_3Fe particles (10–200 μm) in the top layer, and smaller α- Al(Fe, Mn)Si particles (0.1–0.3 μm) throughout the melt pool. Small, partly coherent Al_3Fe precipitates (0.25 μm long) were found between the large Al_3Fe particles. Processing with a defocused laser beam produced a shallower melt pool with a homogeneous distribution of the iron in the form of Al_3Fe particles.

1. Introduction

Ductile materials coated with a hard surface layer should achieve better wear properties and/or better corrosion resistance [1]. Such materials may have good properties for most designing purposes. There are several methods for producing a surface coating on metals: plasma spraying, powder vacuum deposition or heat treatment with a laser. The development of laser technology in recent years has provided new possibilites for surface modification of different materials, and most of the traditional problems with surface coatings are reduced. This includes problems such as adhesion between the surface layer and the substrate, limitations of the thickness of the surface layer, and a precise definition of the surface-modified area [2].

Aluminium is a widely used construction material and will, with a better surface hardness and wear properties, find new areas of usage. Surface modification of aluminium with a laser using alloying elements such as iron, manganese and nickel [3] can induce improvements in hardness and wear properties. This is achieved by strong alloying during melting of the substrate surface. Rapid solidification of the melt in a thin surface layer can give a high concentration of alloying elements in the solid solution and a fine distribution of precipitates. The microstructures and the hardness and wear properties depend strongly on the solidification conditions and have more similarities to melt welding than ordinary casting.

The aim of this study was to investigate surface modification of aluminium coated with plasma-sprayed iron and laser treated using two laser beam settings: integrated and defocused laser beam. The processing parameters were systematically varied for both laser beams.

The microstructures were characterized by optical and electron microscopy while average compositions were measured by electron microprobe analyses and mechanical properties by hardness measurements. The investigation was concentrated on the characteristics connected with the improvements of mechanical properties, in addition to describing the different phases and their faults that occurred due to the rapid quenching. All identifications of the intermetallic phases were based on electron diffraction and X-ray microanalysis in a transmission electron microscope (TEM).

2. Experimental procedure

A 5000-aluminium alloy was plasma sprayed with iron powder on the surface at two different thicknesses, 50 and 100 μm. Plasma spraying was used to ensure adhesion of the iron powder to the aluminium surface during laser treatment with a high-effect CO_2 laser. A doughnut-shaped beam with an outer radius of 50 mm was used which could be focused down to 0.2 mm.

Two different laser-beam settings were used: defocused and integrated. With the defocused laser beam the specimen was placed above the focus, where the beam diameter was 3 mm. The principle of the integrated laser beam generation is shown in Fig. 1. The defocused laser beam is directed towards an integration mirror consisting of 6 by 6 small mirrors at different angles to the laser beam. The beam is then reflected to a spherical mirror which reflects a 12 mm by 12 mm laser beam to the work piece. The process parameters which varied during the laser treatment were the laser-beam effect and the specimen speed (Tables I and II). The processing conditions are quite

---

* *Present address*: SINTEF SI, P.O.Box 124 Blindern, 0314 Oslo, Norway.

0022–2461

different for the integrated and defocused laser beam, owing to the large difference in both beam area ($12 \times 12\ \text{mm}^2$ compared with $\pi(3\ \text{mm})^2$) and interaction time which is four times longer for the integrated than the defocused laser beam. This gives different absorbed power densities for the two laser-beam settings.

2.1. Specimen preparation for material characterization

The different specimens from both the integrated and defocused laser beam were studied by optical microscopy and electron microprobe analysis, and tested by hardness measurements. These specimens were prepared by mechanically grinding and polishing. Large differences in the microstructures were found for the two laser-beam settings, i.e. the depth of the melt pool, the iron distribution in the melt pool and the phases formed in the melt pool.

A selection of specimens was examined by transmission electron microscopy in a JEM 200 CX equipped with a Tracor Northern energy dispersive X-ray analyser. The crystalline phases were identified by selected-area electron diffraction (SAD) and the composition of the particles was determined by X-ray microanalysis. Specimen preparation for these TEM studies was difficult, owing to the variations in hardness and roughness of the specimen surface layer. A preparation method described by Ivey and Piercy [4] was partly used.

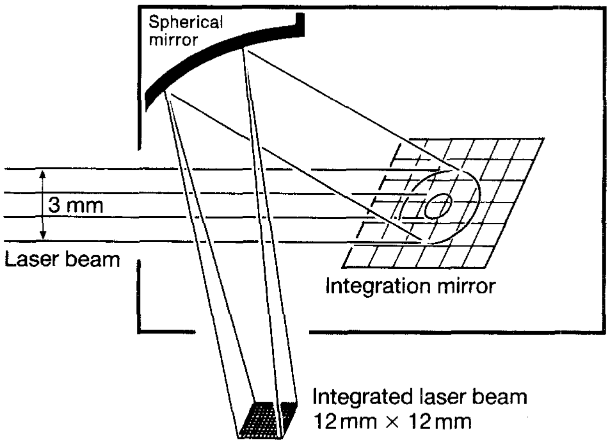

Figure 1 Sketch of integrated laser-beam generation.

2.2. Characterization of the iron powder and the plasma-sprayed coatings

The iron powder and the plasma-sprayed coatings were studied by optical and scanning electron microscopy (SEM). The SEM instrument was a JSM 840.

TABLE I Processing data and results for specimens processed with an integrated laser beam. Specimens 3–9 and 11–15 have 50 and 100 μm plasma-sprayed iron coating, respectively

Specimen	Effect (kW)	Speed (m min^{-1})	Melt pool depth (μm)	Iron depth (μm)	Mean hardness (HV1) of melt pool	Mean hardness (HV1) of HAZ
3	5.6	0.5	1700	108	64.2	74.8
4	5.6	0.25	2000	80	63.9	61.8
6	10.0	0.5	4500	250	66.1	59.7
8	10.0	1.0	1800	50	63.7	75.1
9	10.0	2.0	1350	54	67.8	77.7
11	5.5	0.5	1800	100	65.7	75.4
12	5.5	0.25	1800	160	67.9	76.2
13	10.0	0.5	4600	270	70.2	74.2
14	10.0	1.0	2200	80	62.5	77.1
15	10.0	2.0	1100	40	67.7	76.4

TABLE II Processing data and results for specimens processed with defocused laser beam. All specimens have 100 μm plasma-sprayed iron coating

Specimen	Effect (kW)	Speed (m min^{-1})	Melt pool depth (Iron depth) (μm)	Melt pool width (mm)	Mean hardness (HV1) of melt pool
4	5.5	1.0	370	2.95	356
9	5.5	2.0	480	2.90	
16	5.5	3.4	640	2.92	314
19	5.5	4.0	540	2.92	
20	5.5	5.0	390	2.97	
22	11.0	1.0	890	3.28	248
27	11.0	2.0	900	3.51	
30	11.0	3.0	870	3.47	
32	11.0	4.0	1050	3.48	183
34	11.0	5.0	1320	3.34	
41	11.0	8.0	1110	3.29	159

The powder of spherical particles had a mean diameter of 75 µm and was identified by X-ray diffraction as α-iron. The iron coatings showed a great variation in thickness and varying amounts of iron oxides for different series of plasma spraying. All the coatings had pores within the coating and between the coating and the substrate.

3. Results

3.1. Integrated laser beam

The integrated laser beam gave a deep melt pool with poor mixing of the iron into the aluminium substrate and with a large heat-affected zone (HAZ). The hardness of both the melt pool and the HAZ decreased compared to the aluminium substrate. Results of hardness measurements are given in Table I.

A large variation in the microstructure was found down through the melt pool. The incompletely melted iron coating on the top of the substrate consisted of α-iron and iron oxides.

Small α-Al(Mn, Fe)Si particles were observed by optical microscopy throughout the melt pool, as seen in the lower part of Fig. 2. Both the primitive (space group Pm3, cell dimension $a = 1.252$ nm [5]) and the body centred (space group Im3, cell dimension $a = 1.256$ nm [5]) cubic phases were present, with particles of the body centred generally larger (0.1–3 µm) than the primitive phase (0.1–0.3 µm).

In the uppermost part of the melt pool in Fig. 2, large needle-shaped Al_3Fe particles (10–200 µm, space group C2/m, cell dimensions $a = 1.549$ nm, $b = 0.808$ nm, $c = 1.248$ nm, $\beta = 107.72°$ [5]) were found. These particles gave extensive streaking along $\boldsymbol{c}^*$ in the SAD patterns due to faults on (001) as is often observed in direct casting of aluminium [6].

Between the large Al_3Fe particles, small partly coherent, needle-shaped precipitates were found. The precipitates are 250 nm long, 1–2 nm thick and are oriented along the cube axis of aluminium. SAD revealed diffuse streaks with a strong variation in the intensity. Figs 3a and 4a show streaks oriented in three directions in the reciprocal space parallel to the $\langle hk0\rangle^*$ directions in aluminium. Each precipitate direction in the aluminium matrix is represented by a diffuse plane in reciprocal space normal to $\langle 001\rangle_{Al}$.

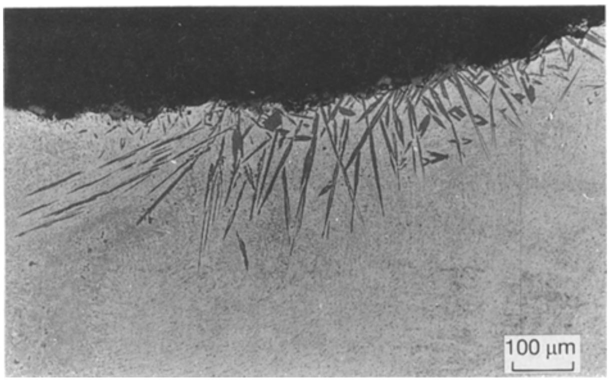

Figure 2 Optical micrograph showing needle-shaped large Al_3Fe particles in the top layer and smaller α-Al(Fe, Mn)Si particles in the lower parts. Integrated laser beam, specimen 6.

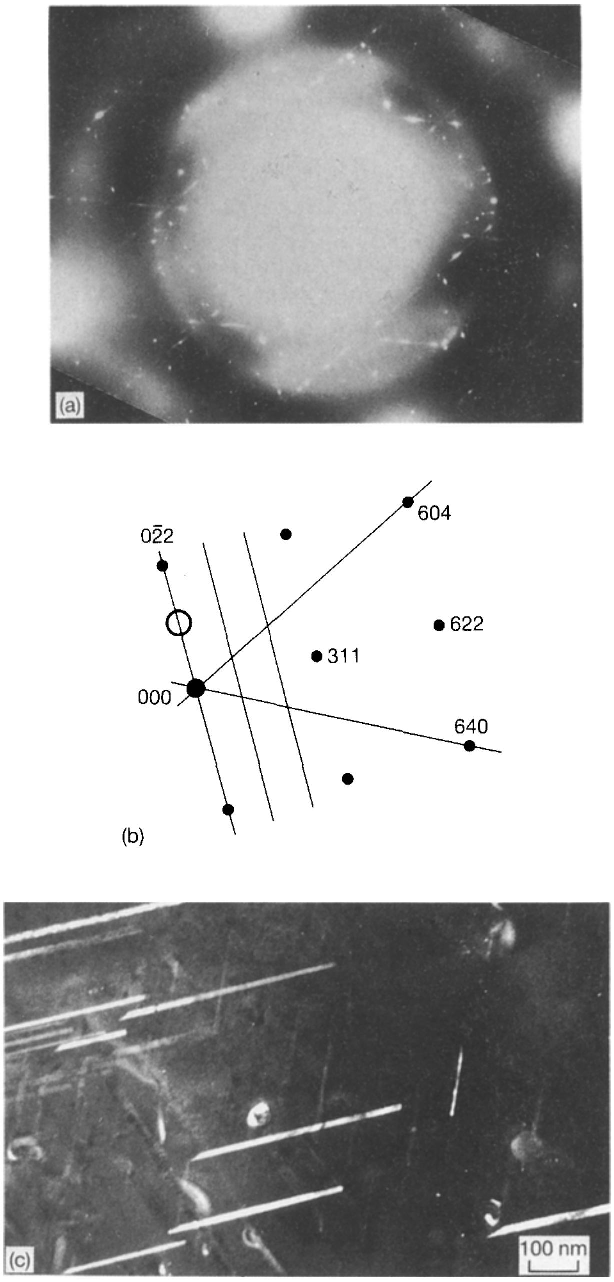

Figure 3 Diffuse streaking from Al_3Fe precipitates due to shape effects. Specimen orientation is [$\bar{2}$33]. (a) SAD pattern, (b) indexing and some of the diffuse streaks and (c) DF image obtained with the Al_3Fe reflection at the aluminium position 0$\bar{1}$1. Specimen 11, integrated laser beam.

The intersection between these planes and the Ewald sphere will give streaks in the SAD patterns. This means that for each $\langle 001\rangle_{Al}$ direction, we obtain a set of diffuse streaks along the $\langle hk0\rangle^*_{Al}$ directions. Fig. 3c shows a dark-field (DF) image taken from the aluminium position 0$\bar{1}$1, where only the diffuse streak in the [0$\bar{2}$2] direction has an intensity maxima and only the precipitates normal to this direction is revealed in the DF image. The DF image in Fig. 4c is taken from the aluminium position $\bar{2}$22, where all the three diffuse streaks have intensity maxima and the precipitates along all the three cube axis are shown in the DF image. Fig. 5 shows the set of diffuse streaks due to intersections between the Ewald sphere, and the reciprocal diffuse planes normal to the directions of the precipitates. Note that all $\langle hk0\rangle^*_{Al}$ directions are

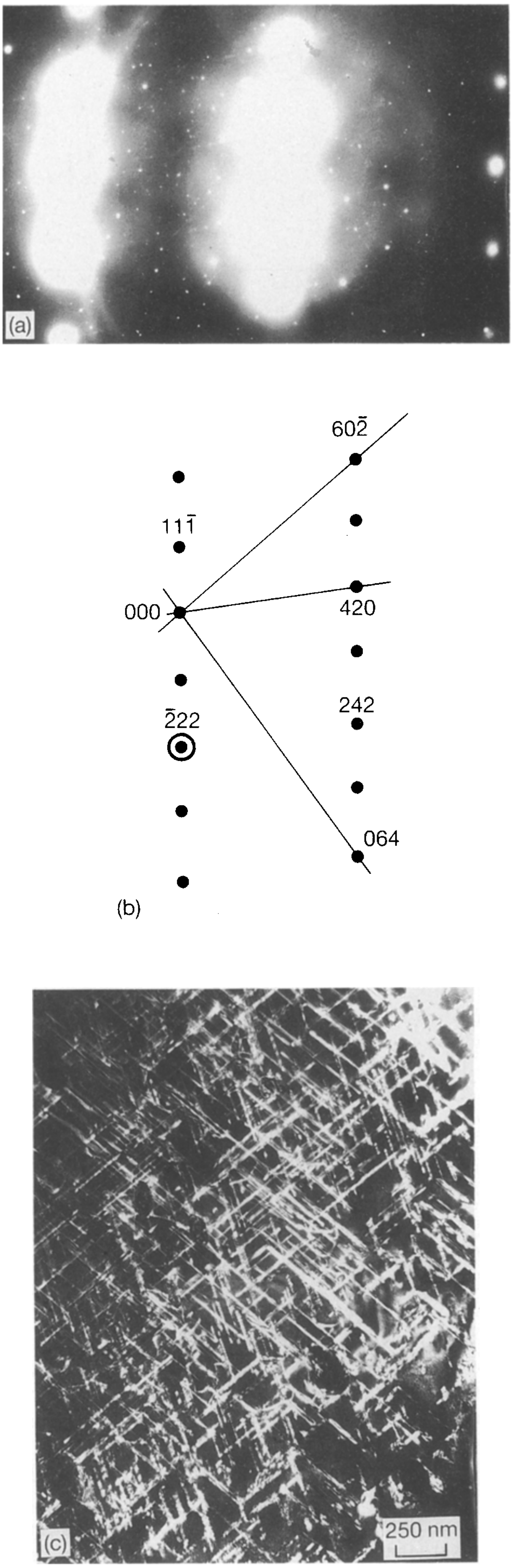

Figure 4 Diffuse streaking from Al_3Fe precipitates due to shape effects. Specimen orientation is $[1\,\bar{2}\,3]$. (a) SAD pattern, (b) indexing and some of the diffuse streaks, and (c) DF image obtained with the Al_3Fe reflection at the aluminium position $\bar{2}22$. Specimen 11, integrated laser beam.

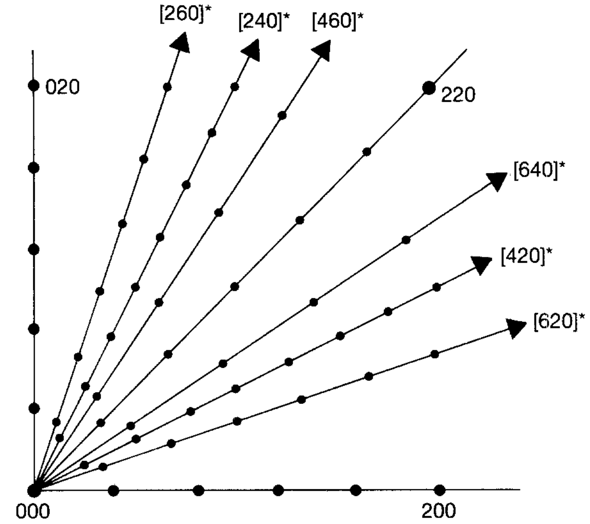

Figure 5 Position of intensity maxima along the diffuse streaks from Al_3Fe precipitates. Indexing according to aluminium.

considered equivalent. The intensity maxima along the diffuse streaks give a network of diffraction spots between the reciprocal aluminium lattice. Along $\langle 4\,2\,0\rangle^*_{Al}$ in aluminium the intensity maxima give a spacing which is close to a doubling of $\boldsymbol{a}^*$ in Al_3Fe and along $\langle 2\,6\,0\rangle^*_{Al}$ a spacing close to $\boldsymbol{c}^*$. We achieve a reciprocal diffuse plane spanned by $\boldsymbol{a}^*_{Al_3Fe}$ and $\boldsymbol{c}^*_{Al_3Fe}$ normal to the length of the precipitates. $\boldsymbol{b}_{Al_3Fe}$ is therefore parallel to the length of the precipitate. $\boldsymbol{b}_{Al_3Fe} = 0.808$ nm and is comparable to a doubling of the aluminium cube axes $a_{Al} = 0.404$ nm. Because aluminium is centrosymmetric (space group $Fm\bar{3}m$), the $\boldsymbol{b}_{Al}$ and $-\boldsymbol{b}_{Al}$ directions are equivalent. According to the space group symmetry ($C2/m$) of Al_3Fe, the $[h\,0\,l]_{Al_3Fe}$ and $[\bar{h}\,0\,\bar{l}]_{Al_3Fe}$ directions are equivalent due to the two-fold axis along $\boldsymbol{b}_{Al_3Fe}$. Therefore, when the space group symmetries of aluminium and Al_3Fe are taken into account, there are four possible orientations of an Al_3Fe unit cell along each cube axis in aluminium.

3.2. Defocused laser beam

This laser-beam setting produced a clear improvement of hardness as can be seen by comparing the hardness values in Tables I and II. A defocused laser beam gave a shallow melt pool with homogeneous distribution of the iron in the melt pool and a small HAZ. The iron in the melt pool appeared as Al_3Fe particles. Figs 6 and 7 show that the amount and density of the particles vary strongly with the depth of the melt pool. This is quite reasonable, because the concentration of aluminium increases with increasing melt pool depth. As shown in Fig. 8 the microhardness decreases with increasing depth. Therefore, there is a simple correlation between the microhardness and the particle density. In the most shallow melt pools, local microhardness up to 600–700 HV0.1 was measured.

The Al_3Fe particles were heavily twinned as revealed by extensive streaking and splitting of reflections in $\boldsymbol{c}^*$ directions (Fig. 9). For h and k even the matrix and twin reflections coincide. The twinning was of the rotation type with $[0\,0\,1]^*$ as the twin axis.

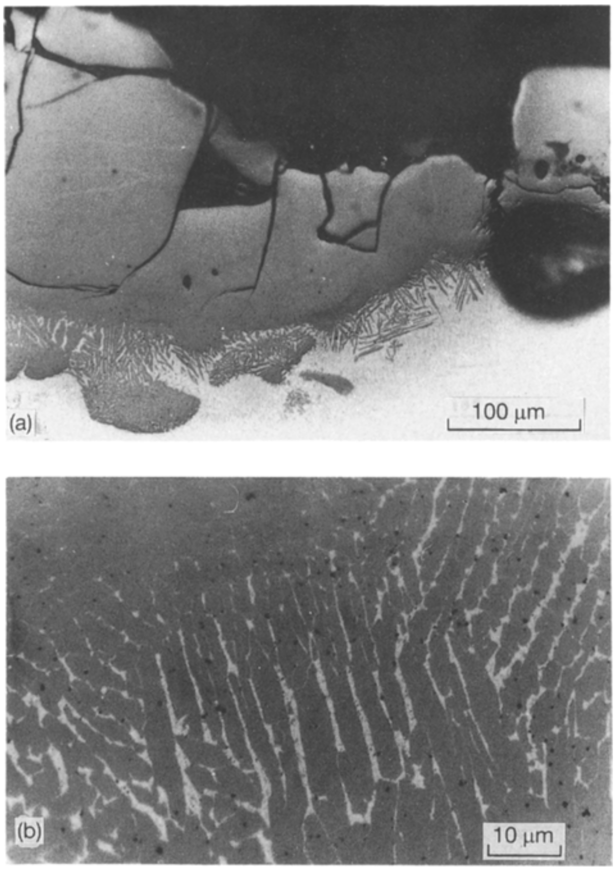

Figure 6 Optical micrographs showing the density and amount of Al_3Fe particles in specimen 4, defocused laser beam; (a) low magnification, (b) high magnification.

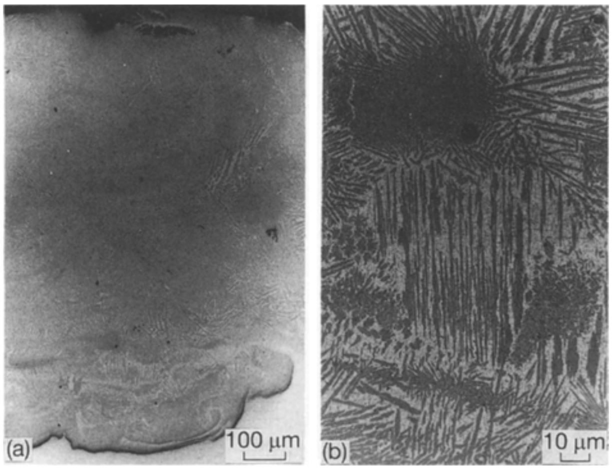

Figure 7 Optical micrographs showing the density and amount of Al_3Fe particles in specimen 41, defocused laser beam; (a) low magnification, (b) high magnification.

The twinning was directional and uniform across large specimen areas. The spacing of the twins varies with process parameters and thus with depth of the melt pool. As shown in Fig. 9a and b the shallow melt pool resulted in wider twins which gave distinct splitting of reflections, while samples from the deeper melt pool showed almost continuous streaking due to finer twins as seen in Fig. 9c and d.

Particles with [1 0 0]* rotation twins were also found, but these are not as frequent as the particles with rotation twinning on [0 0 1]*.

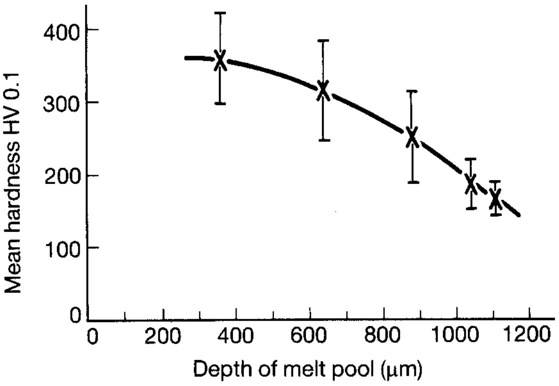

Figure 8 Mean hardness versus depth of melt pool from specimens processed with the defocused laser beam.

In the most shallow melt pool, a relatively large iron content of Al_3Fe particles was found by X-ray microanalysis. This is apparently related to the large twins and the increase in average iron content in the melt as the depth of the melt pool decreases. Several X-ray spectra were taken to verify the iron content of 35 at % in the Al_3Fe particles, after effects of absorptions and fluorescence had been taken into account and corrected for.

3.3. Temperature and solidification calculations

Temperature gradients and solidification rates were estimated by computer calculations following essentially a modified Rosenthal equation where the equations used are given by Kear, Mayer, Poate and Strutt [7]. Temperature evolution in the melt pool during heating and cooling is given by Equations 5 and 6 in reference [7], the temperature gradient is given by Equation 9 [7] and the solidification rate is given by Equation 11 [7]. Because most of the specimens have composition close to the aluminium-rich part of the Al–Fe phase diagram, the iron coating was not included in these calculations. Therefore, the material constants are taken as for pure aluminium. This gives a conductivity of $2.29\ \mathrm{W\,cm^{-1}K^{-1}}$ and a diffusivity of $0.85\ \mathrm{cm^2\,s^{-1}}$, the initial temperature is taken as 20 °C. The calculations were executed on one specimen from each laser-beam setting, and the absorbed power densities were accordingly: specimen 9, integrated laser beam, $6.94\ \mathrm{kW\,cm^{-2}}$, and specimen 22, defocused laser beam, $38.9\ \mathrm{kW\,cm^{-2}}$.

The calculations (Figs 10 and 11) illustrate the difference between the integrated and defocused laser beams. The maximum surface temperature with integrated laser beam (Fig. 10a) was below the melting temperature for iron (1536 °C). On the other hand, with the defocused laser beam the maximum surface temperature (Fig. 11a) was well above 1536 °C and ensured a complete melting of the iron coating. Latent heat in the melt pool will cause an increase in temperature after the interaction time, as seen in Figs 10a and 11a, before the cooling and solidification of the surface layer can start. There is an increased solidification rate towards the surface of the specimen (Figs 10b and 11b), which is also seen in Figs 6 and 7 as a finer

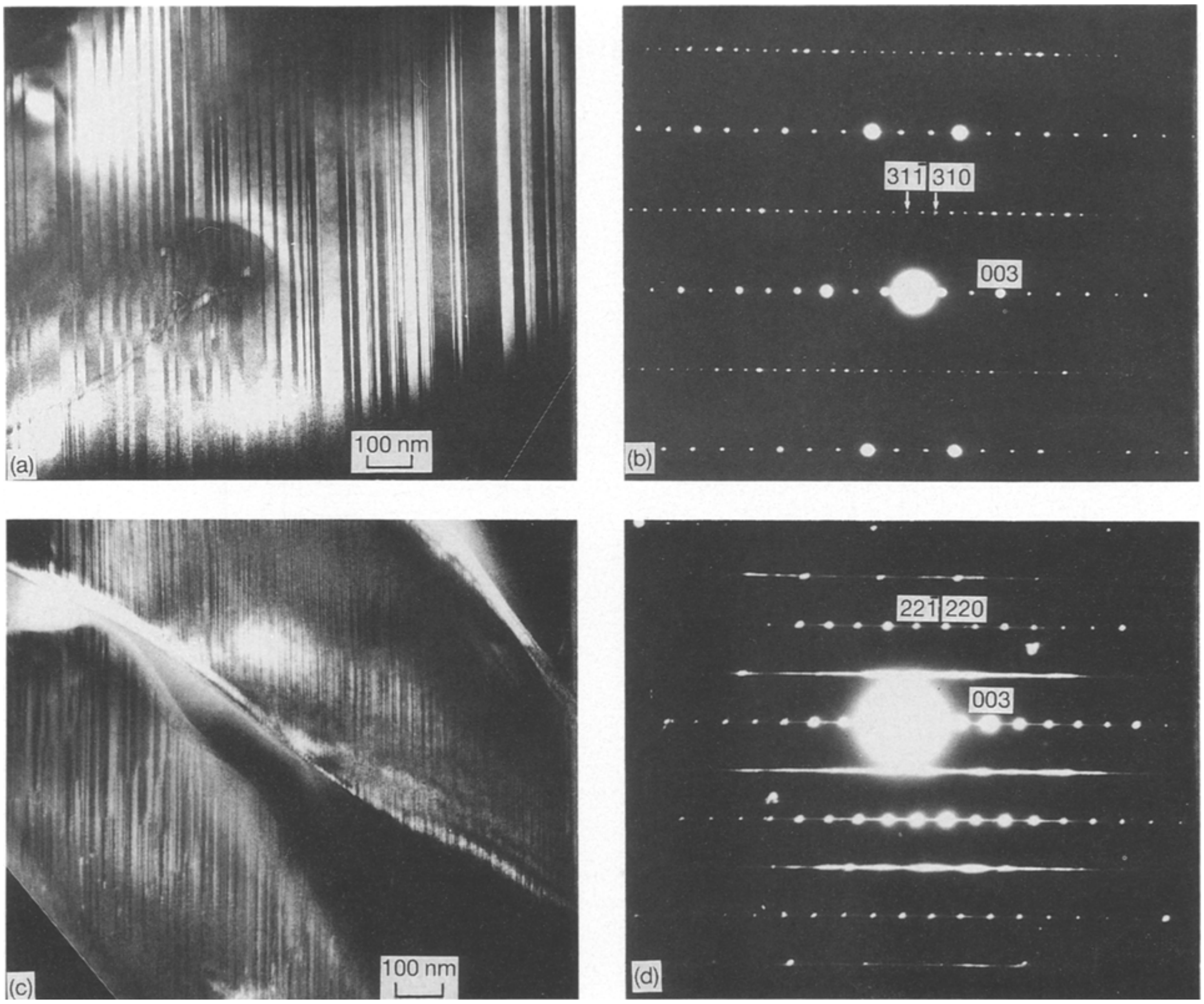

Figure 9(a, c) DF images of twins and (b, d) corresponding SAD patterns. (a, b) Specimen 4 with crystal orientation $[1\,\bar{3}\,0]$. (c, d) Specimen 32 with crystal orientation $[1\,\bar{1}\,0]$.

dendritic structure towards the surface. Figs 10b and 11b also show that a constant solidification rate is achieved at a given depth of the melt pool shortly after the interaction time. This time interval decreases towards the surface. The temperature gradients (Figs 10c and 11c) are lower at the surface and there is a high gradient in the initiation of the cooling. Specimens processed with the integrated laser beam have a much lower temperature gradient than those processed with the defocused laser beam.

4. Discussion

The two different laser-beam treatments of iron-coated aluminium substrate produced surface coatings with quite different properties.

4.1. Integrated laser beam

The surface modification with integrated laser beam gave an incomplete melting of the iron coating and inhomogeneous distribution of the iron throughout the aluminium melt. The aluminium was melted to a large depth (1000–6000 μm) with a wide HAZ. The hardness was reduced both in the melt pool as well as in the HAZ compared to the aluminium substrate. Investigations of the microstructure by TEM revealed large Al_3Fe particles in the uppermost layer and α-Al(Mn, Fe)Si particles distributed throughout the melt pool, as well as small needle-shaped Al_3Fe precipitates between the larger Al_3Fe particles. These precipitates are partially coherent and oriented along the cube axis of aluminium. The diffuse streaking revealed by SAD is explained as due to three sets of diffuse planes perpendicular to each orientation of precipitates. Each set of diffuse streaks is due to the intersection between the Ewald sphere and a diffuse reciprocal plane spanned by $\boldsymbol{a}^*_{Al_3Fe}$ and $\boldsymbol{c}^*_{Al_3Fe}$. This plane is normal to $\boldsymbol{b}_{Al_3Fe}$ which is parallel to the length of the precipitates.

Coherence is found between precipitate and matrix perpendicular to the needle-shaped precipitates. This coherence is obtained due to the relationship $\boldsymbol{a}_{Al} = 1/2\boldsymbol{b}_{Al_3Fe}$. The Al_3Fe unit cell consists of four layers normal to $\boldsymbol{b}$ [6]. There are two flat layers at $y = 0$ and 0.5 where the layer at $y = 0.5$ is displaced $1/2[1\,0\,0]$ relative to the layer at $y = 0$. There are two puckered layers at $y = 0.25$ and 0.75 with a displacement vector $1/2[1\,0\,0]$. By introducing a displacement $1/2[1\,0\,0]$ in the two flat layers, $y = 0$ and 0.5, they will be equivalent, and we will achieve perfect coherence at the precipitate/matrix interface as observed. The unit cell

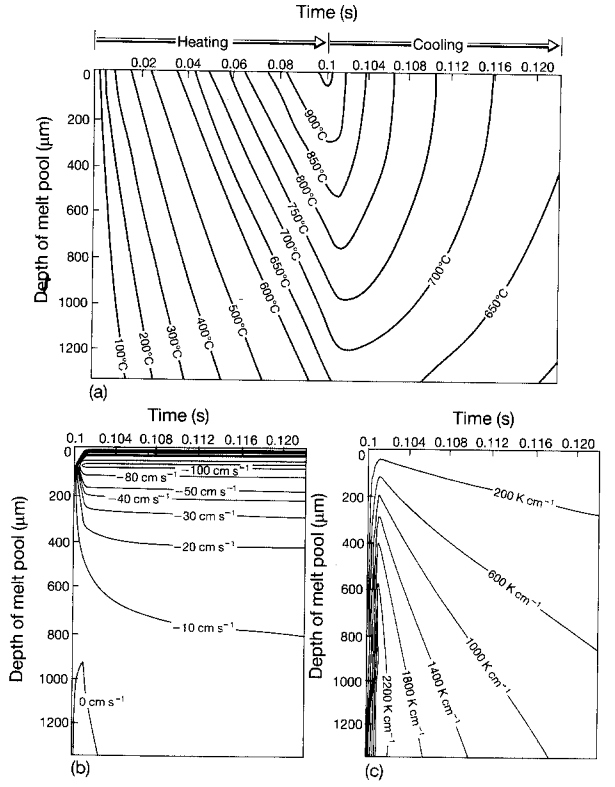

Figure 10 Calculations for integrated laser beam, specimen 9: (a) temperature during heating and cooling of the surface coating, (b) solidification rate, and (c) temperature gradient during cooling.

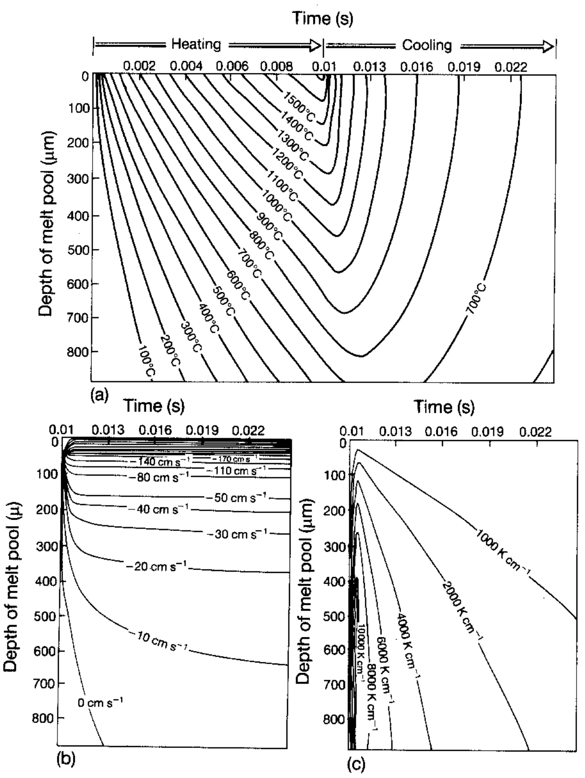

Figure 11 Calculations for defocused laser beam, specimen 22: (a) temperature during heating and cooling of the surface coating, (b) solidification rate, and (c) temperature gradient during cooling.

of these precipitates is then described by two equal units along b_{Al_3Fe}, modified from the Al_3Fe unit cell.

Blank [8] and Adam and Bourdeau [9] have reported similar precipitates, θ-precipitates (Al_3Fe) which are partially coherent to the aluminium matrix. They found that ***b*** was parallel to the cube axis in aluminium. Their findings were done on material being heat treated and where a θ′-phase partially coherent to matrix was transformed into the θ-phase. The observations by Blank [8] and Adam and Bourdeau [9] seem to be in accordance with the results and the conclusions drawn from the present work.

4.2. Defocused laser beam

The defocused laser beam produced a shallower melt pool (300–1100 µm) where the iron was completely dissolved in the aluminium and homogeneously distributed throughout the melt pool. The hardness of the surface layer increased heavily. Local values up to 700 HV0.1 were measured in the shallowest melt pool. The increase in hardness, as shown in Table II is clearly connected to the iron concentration in the melt pool and the density of particles which again is given by the depth of the melt pool. TEM studies showed Al_3Fe particles with a large content of [0 0 1]* rotation twins. The Al_3Fe particles in the deeper melt pools showed finer twins, which resemble the structure of Al_3Fe particles found in ordinary casting [6]. The shallower melt pools gave Al_3Fe particles with wider twins and higher iron content. This is apparently due to the high iron concentration in the melt during laser treatment, as well as the high solidification rate of the melt pool.

5. Conclusion

The different surface coatings achieved with the two laser-beam settings, have very different characteristics.

The integrated laser beam has a low energy density and a long interaction time which leads to a large spread of heat in the material. We achieved deep melt pools with an incomplete melting of the plasma-sprayed iron coating. On the other hand, the defocused laser beam gives a much higher energy density and a shorter interaction time and shallower melt pools were obtained with a homogeneous mixing of the iron into the aluminium.

The incomplete melting of the iron coating with integrated laser beam results in an inhomogeneous distribution of iron in the melt pool, as large Al_3Fe particles in the top layer. No increase in hardness of the surface coating for these specimens was observed. The defocused laser beam gives a homogeneous distribution of the iron which appears as heavily twinned Al_3Fe particles, whereas the special solidification conditions produce a variation in twin spacing with melt pool depth. There is a clear increase in hardness of the surface coating with decreasing melt pool depths. This gives an improvement of the surface qualities of the aluminium substrate.

A combination of introductory experiments and calculations can be very useful in optimizing the conditions for laser-surface modification.

Acknowledgements

The authors thank Svein Ove Olsen, SINTEF SI, for help with plasma spraying and laser treatment, and Erik Sørbrøden, Center for Materials Research, University of Oslo, for help with the transmission electron microscopy.

References

1. C. W. DRAPER and J. M. POATE, *Int. Met. Rev.* **30** (1985) 85.
2. G. J. BRUCK, *Proc. SPIE* **957** (1988) 14.
3. E. GAFFET, J. M. PELLETIER and S. BONNET-JOBEZ, *Acta metall.* **37** (1989) 3205.
4. D. G. IVEY and G. R. PIERCY, *J. Electron Microsc. Tech.* **8** (1988) 233.
5. P. VILLARS and L. D. CALVETT, "Pearson's Handbook of Crystallographic Data for Intermetallic Phases" (American Society for Metals, Ohio, 1985).
6. P. SKJERPE, Doctoral Thesis, University of Oslo, Norway (1989).
7. B. H. KEAR, J. W. MAYER, J. M. POATE and P. R. STRUTT, in "Metallurgical Treaties", edited by J. K. Tien and J. F. Elliott (Metals Society, London, 1981) p. 321.
8. E. von BLANK, *Z. Metallkde* **63** (1972) 324.
9. C. M. ADAM and R. G. BOURDEAU, in "Proceedings of the Second International Conference on Rapid Solidification Processing", edited by R. Mehrabian, B. H. Kear and M. Cohen (Claitor, Baton Range, 1980) p. 246.

Received 3 November 1992
and accepted 28 July 1993